ELSEVIER

Journal of Fluids and Structures 22 (2006) 961–971

JOURNAL OF FLUIDS AND STRUCTURES

www.elsevier.com/locate/jfs

# Instability of the flow around an impacting sphere

T. Leweke[a,*], M.C. Thompson[b], K. Hourigan[b]

[a]*Institut de Recherche sur les Phénomènes Hors Equilibre (IRPHE), CNRS/Universités Aix-Marseille, 49 rue Frédéric Joliot-Curie, B.P. 146, F-13884 Marseille Cedex 13, France*

[b]*Fluids Laboratory for Aeronautical and Industrial Research (FLAIR), Department of Mechanical Engineering, Monash University, VIC 3800, Melbourne, Australia*

Received 12 May 2006; accepted 22 May 2006
Available online 28 July 2006

**Abstract**

Results from an experimental and numerical study of the flow generated by a sphere immersed in fluid, impacting normally without rebound on a solid wall, are presented. The parameters are the running distance before impact and the sphere Reynolds number. For running lengths less than 7.5 diameters, the sphere wake before impact is axisymmetric in the form of an attached vortex ring. After impact, this ring overtakes the sphere and spreads out along the wall. For Reynolds numbers below 1000, the flow remains axisymmetric at all times. For higher values, perturbations of azimuthal wavenumbers 20–25 are observed on the vortex ring, leading to a breakdown of the flow. We analyse different hypotheses concerning the origin of this instability, with the conclusion that a centrifugal instability mechanism is likely to be acting in this flow. Comparisons are made with the flow involving an isolated vortex ring approaching a wall. Numerical simulations of this case have revealed that two distinct instability mechanisms are operating, one of which appears to be similar to the centrifugal instability observed for the sphere impact.


## 1. Introduction

This article deals with the flow generated by a sphere impacting a solid wall without a rebound. Such a configuration has potential relevance for the determination of wall heat exchange properties in the presence of particles, due to the convection of fluid towards and way from the surface by the flow generated by the impact, as well as for the problem of resuspension of dust from the surface. For spherical solid bodies impacting on a wall, the wake flow following the body overtakes it on impact, and the resultant vortex ring structure(s) can cause significant fluid exchange near the surface. Eames and Dalziel (2000) have examined this behavior in detail, as the Reynolds number was varied between 300 and 3500. In that study, the analysis was primarily directed towards resuspension characteristics of different dust types and layer thicknesses, rather than the fluid dynamics, which is of primary concern in the present study. Joseph et al. (2001) experimentally examined particle-wall collisions for Reynolds numbers between 10 and 3000, and showed that the rebound was primarily a function of the Stokes number. Both Joseph et al. (2001) and Gondret et al. (2002) determined the coefficient of restitution as a function of Stokes number and showed that it reaches an asymptotic value for high Stokes numbers, corresponding to the value for 'dry' collisions. The vortex ring system

*Corresponding author.
*E-mail address:* Thomas.Leweke@irphe.univ-mrs.fr (T. Leweke).

0889-9746/$ - see front matter © 2006 Elsevier Ltd. All rights reserved.
doi:10.1016/j.jfluidstructs.2006.05.002

generated after the impact of a solid body shows similarities to that produced from the collision of a vortex ring with a wall, examined by a number of authors including, e.g., Walker et al. (1987), Orlandi and Verzicco (1993) and Swearingen et al. (1995).

It is known from previous work (Eames and Dalziel, 2000; Leweke et al., 2004) that the vortex ring spreading along the wall after impact undergoes a three-dimensional (nonaxisymmetric) instability for Reynolds numbers exceeding approximately 1000, leading to a rapid disintegration of the vortex. After recalling the main features of the flow in the axisymmetric regime below this threshold, the paper focuses on the following two aspects of the particle-wall interaction: the physical basis for the three-dimensional instability, and a comparison of this instability with the one observed for typical isolated vortex ring impacts. These analyses are based on the results of a combined experimental-numerical study, described briefly in the following section.

## 2. Technical details

### 2.1. Experiments

The experiments were carried out in a $50 \times 50 \times 60\,\mathrm{cm}^3$ water tank with a plexiglas bottom, using a bronze sphere of diameter $D = 19\,\mathrm{mm}$ attached to an inelastic string, and whose vertical motion was imposed by a computer-controlled stepper motor. Visualization was achieved using fluorescent dye, painted on the sphere surface prior to lowering it into the water to its initial position, and illuminated by the light from an Argon laser. The sphere was impulsively started from rest at a distance $L$ from the bottom surface. It moved downward with constant speed $U$ until it just touched the surface, where its motion was stopped without rebound (see Fig. 1). Time $t$ is counted from the impact and non-dimensionalised as $\tau = tU/D$. More details on the experimental set-up and procedure are given in Thompson et al. (2006).

### 2.2. Numerical simulations

Existing spectral-element software [see, e.g., Thompson et al. (2001) and Sheard et al. (2003)] was modified to perform direct numerical simulations (DNS). The movement of the sphere relative to the wall was treated using the Arbitrary Lagrangian Eulerian approach (Warburton and Karniadakis, 1997). As the sphere moves towards the surface, the vertices of the mesh move with predetermined specified velocities, so that the semi-circular boundary of the sphere (in the axisymmetric coordinate system) is maintained and the distortion of the mesh is controlled. The sphere was stopped at $0.005D$ away from the wall to avoid the development of a mesh singularity over the final few time steps before impact. The nondimensional parameters controlling the interaction are the Reynolds number of the sphere during its motion, $\mathrm{Re} = UD/\nu$, where $\nu$ is the kinematic viscosity, and the rescaled running length $L/D$.

For the analysis in Section 5, DNS of a vortex ring approaching a wall was carried out using a fixed grid. The vortex ring initially has circulation $\Gamma$ and a Gaussian vorticity distribution with a characteristic core radius $a$. The initial diameter of the ring centreline is $2A$, and at $t = 0$ it is located at a height $2A$ above the solid wall. In this case, the nondimensional parameters are the circulation Reynolds number $\mathrm{Re}_\Gamma = \Gamma/\nu$ of the vortex ring, and the rescaled core size $a/A$. The nondimensional time is here defined by $t^* = t\Gamma/A^2$.

## 3. Axisymmetric flow

Fig. 2 shows the evolution of the flow generated by an impacting sphere for $\mathrm{Re} = 800$ and $L/D = 5$. For this parameter set, the flow remains axisymmetric throughout the evolution (as confirmed by Fig. 2(d)), yet the Reynolds number is sufficiently large to allow a complex vortex ring system to develop. The left-hand side of images (a)–(c) are experimental dye visualizations, and the right-hand side shows instantaneous fields of azimuthal vorticity, obtained from DNS simulations, together with positions of tracer particles placed initially in a layer near the wall. The visualizations clearly show the wake vortex behind the sphere at impact. A small secondary vortex develops from the opposite-signed vorticity generated on, and shedding from, the sphere surface as the wake vortex ring threads over the sphere. The simulations further show the presence of considerable secondary vorticity induced at the wall when the primary vortex ring strikes it. This secondary vorticity wraps around the primary vortex ring, which reduces the total circulation of the structure to very low values, and results in a considerable

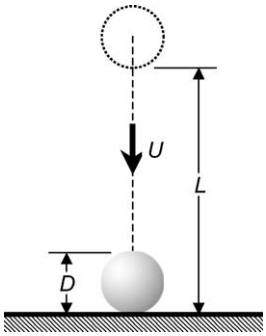


Fig. 1. Schematic of the flow problem studied.

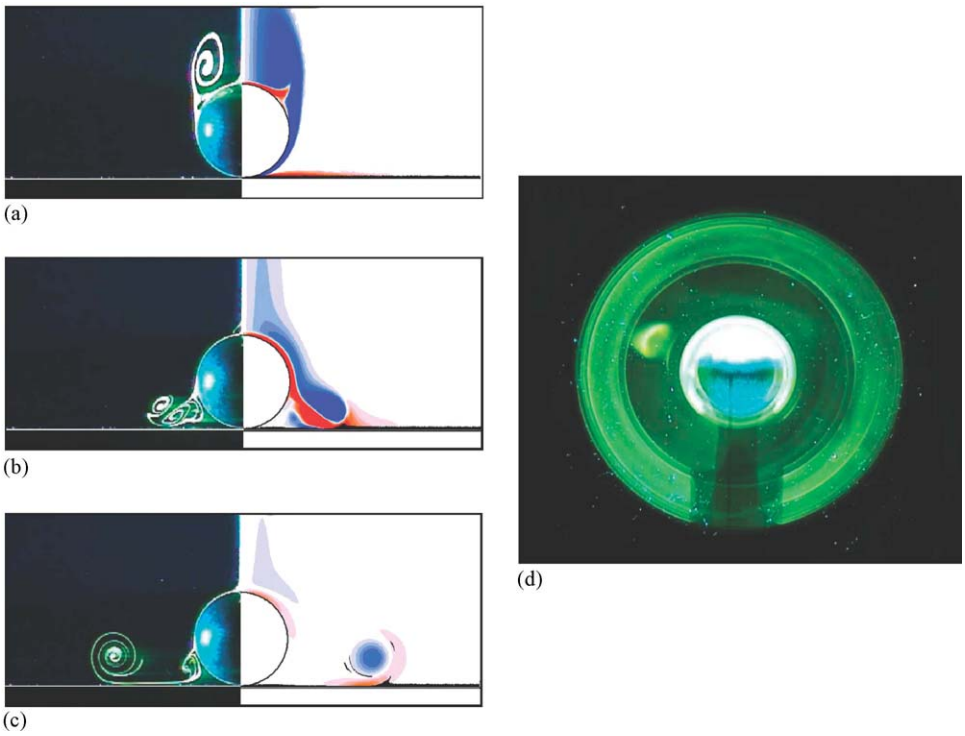


Fig. 2. Flow after impact of the sphere for $\mathrm{Re} = 800$ and $L/D = 5$. (a)–(c) show the flow in a plane passing through the sphere centre, with dye visualization on the left and vorticity and tracer particles from DNS on the right. (a) $\tau = 0$, (b) $\tau = 2$, (c) $\tau = 10$. (d) Dye visualization of the flow at $\tau = 20$, seen from below.

slowing down of the radial spreading of the ring through induction by its image. The primary vortex reaches a final diameter of around $3D$, which varies little throughout the axisymmetric vortex ring regime, i.e., for $2 < L/D < 7.5$ and $500 < \mathrm{Re} < 1000$.

When the running distance $L/D$ of the sphere is varied at constant Reynolds number $\mathrm{Re} = 800$, it is found that the wake before impact, and subsequently the flow throughout the entire evolution, is axisymmetric up to $L/D = 7.5$. For larger distances, the wake vortex ring becomes tilted before the impact, resulting in large-scale perturbations of the later flow. For $L/D < 2$, the wake of the sphere does not have enough time to roll up into a vortex ring, and no coherent structures are observed after impact.

More details about the axisymmetric regime of the sphere impact are given in Thompson et al. (2006).

## 4. Three-dimensional instability

### 4.1. Structure of the instability

When the Reynolds number is increased above a critical value of around 1000, keeping the running distance constant at $L/D = 5$, the flow loses its axisymmetry through an instability occurring after the sphere impact, when the primary wake vortex ring starts spreading out at the wall. Fig. 3 shows this phenomenon, as observed in experiment, in a view from below. The close-up images in Fig. 4 reveal that the perturbations first appear in the outer layers of the primary vortex ring, a certain distance away from its centreline, which still remains relatively unperturbed at this stage. They develop into perpendicular secondary vortices that wrap around the primary one, leading to a breakdown of the vortex ring system at later times. The azimuthal wavenumber of the unstable mode is between 21 and 24.

### 4.2. Physical mechanisms

#### 4.2.1. Deformation of secondary vortex ring

Similar observations of the vortex ring instability were made in the dust resuspension study by Eames and Dalziel (2000). They suggested that the origin of this instability is the same as the one responsible for the three-dimensional instability of the flow generated by a vortex ring impinging on a wall, as explained by Swearingen et al. (1995), namely a combination of self- and mutual induction between the primary ring and a secondary vortex ring of opposite circulation rolling up from the wall vorticity. However, the wavenumbers predicted from this analysis are significantly lower (around 6) than observed in the present study. In addition, the visualizations and numerical results in Fig. 2 show no coherent and discrete secondary vortex structures forming from the wall vorticity for the chosen parameter set. (The qualitative features of the base flow vary little with Reynolds number, even above 1000, although this is addressed in more detail later in Section 5 below).

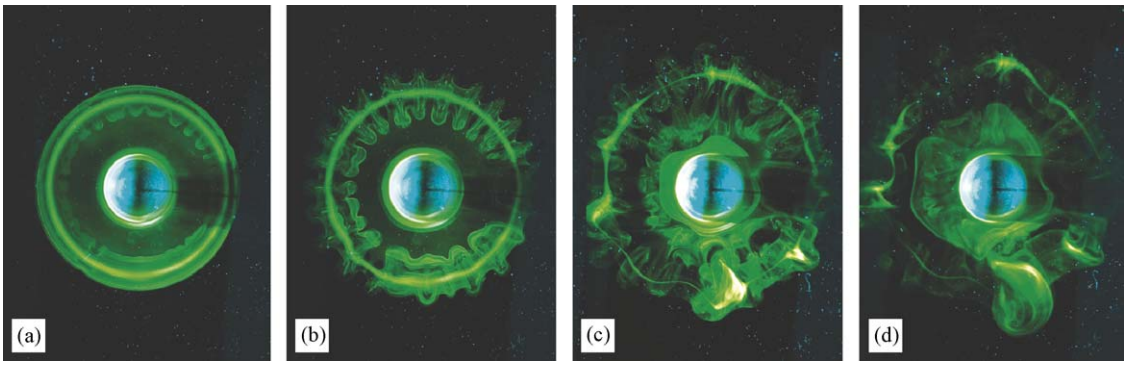


Fig. 3. Sequence of dye visualizations showing the long term evolution of the three-dimensional structure of the vortical ring system for $\mathrm{Re} = 1500$ and $L/D = 5$. (a) $\tau = 4$, (b) $\tau = 9$, (c) $\tau = 20$, (d) $\tau = 40$.

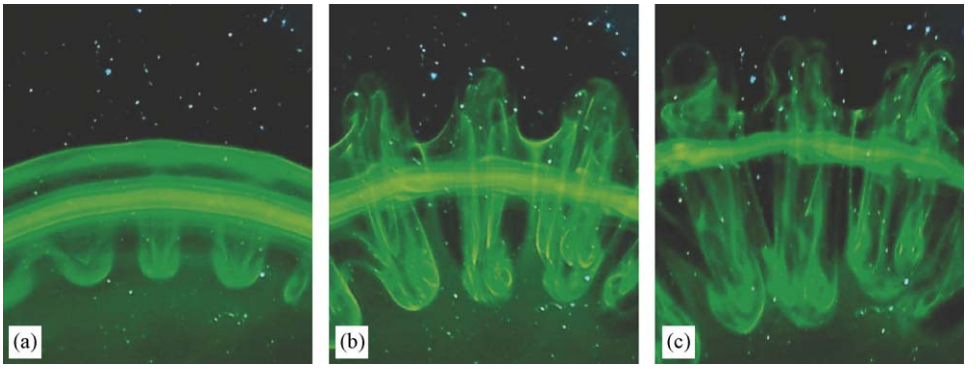


Fig. 4. Close-up view of the development of the secondary vortices for $\mathrm{Re} = 1500$ and $L/D = 5$. (a) $\tau = 4$, (b) $\tau = 9$, (c) $\tau = 14$.

*4.2.2. Elliptic instability of the primary vortex ring*

For the flow situation analysed here, the perturbation field distribution within the core, given in Fig. 5, shows a resemblance with the one expected for the instability of a strained isolated elliptical vortex [see Kerswell (2002) for a review of elliptic instability]. In order to further investigate this idea, analytical theory can be used to examine the axisymmetric 'base flow' for a parameter set (and at a time) for which the perturbations are first observed. Fig. 6(a) shows the case chosen here. According to the work of Eloy and Le Dizès (1999) on the stability of Gaussian-type vortices (which is a good approximation for the vorticity distribution of the inner part of the primary vortex), the most unstable wavelength is close to 2.5 times the radius $r_m$ of maximum swirl velocity $v_\varphi$ (see Fig. 6(a) for notations). With $r_m = 0.112D$ (Fig. 6(b)) and a ring radius $R_v = 1.25$, determined from the DNS results, this leads to a preferred azimuthal wavenumber of $m \approx 28$, consistent with the observed wavelength. The growth rate $\sigma$ of this mode can be estimated, using the same inviscid theory and including a viscous correction (Landman and Saffman, 1987), as: $\sigma D/U = (9/16)(\varepsilon U/D) - 4m^2/(R_v^2 \mathrm{Re})$, where $\varepsilon$ is the strain rate at the centre of the vortex. With $\varepsilon D/U = 0.6$, the predicted growth rate is $\sigma D/U = -1.3$, i.e., clearly negative. This is further supported by a numerical stability analysis of the velocity field associated with *only* the vorticity of the primary vortex core, showing stability of the flow. Hence, on its own, the elliptical instability mechanism does not appear to be sufficient to explain the observed transient growth.

*4.2.3. Centrifugal instability*

The negative vorticity wrapping around the positive-vorticity primary wake vortex creates a flow which appears to be centrifugally unstable. This proposition is also consistent with the observation that the main perturbations are found in the outer part of the vortex, as shown in Fig. 4. Further evidence is again found by analysing theoretically the primary

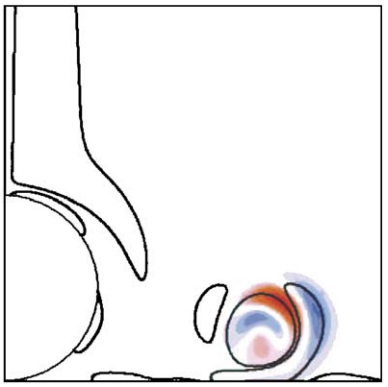

Fig. 5. Perturbation vorticity field at $\tau = 10$ obtained from a direct simulation using low level white noise to perturb the initial axisymmetric field. The position of the primary and secondary azimuthal vorticity is marked by the solid lines. $\mathrm{Re} = 1200$, $L/D = 5$.

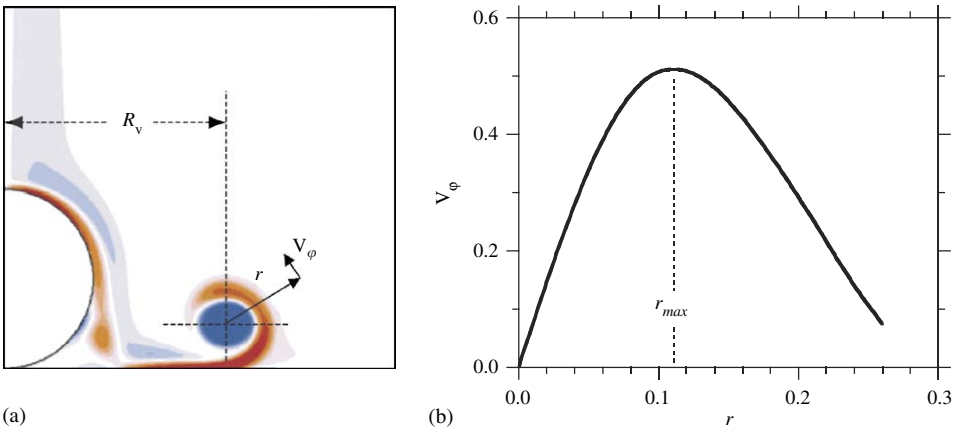


Fig. 6. Analysis of the flow field for $\mathrm{Re} = 1200$ and $L/D = 5$ at $\tau = 4$. (a) Actual azimuthal vorticity distribution, (b) idealized axisymmetric velocity profile of the primary vortex, obtained from an average over $\varphi$ at each $r$, in coordinates centred on the core.

wake vortex flow field for parameters for which the instability sets in. As in the previous section, we consider the flow for $\mathrm{Re} = 1200$ and $L/D = 5$ at $\tau = 4$, shown in Fig. 6(a), and the corresponding azimuthally averaged velocity profile of the primary vortex ring in Fig. 6(b).

Bayly (1988) has presented a generalised theory of centrifugal instability in flows with closed streamlines, and in particular in axisymmetric flows. For inviscid flow, a sufficient condition for a three-dimensional centrifugal-type instability of an axisymmetric flow is that the so-called Rayleigh discriminant, defined as

$$\Phi(r) = \frac{1}{r^3}\frac{\partial}{\partial r}(r^2 v_\varphi^2), \tag{1}$$

becomes negative somewhere in the flow. A 'local' inviscid growth rate $s$ is then given by $s = (-\Phi)^{1/2}$. The region of unstable flow is located where the vorticity changes sign with respect to the vortex core, which is in agreement with the spatial structure of the perturbation observed from direct simulation (Fig. 5).

Furthermore, an estimate for the global growth rate $\sigma$ of the flow can be obtained, following Bayly (1988), by considering two additional effects attenuating the inviscid local growth. The first is a requirement that the perturbations associated with a centrifugal instability fit into the unstable region, which basically impose a cut-off at lower azimuthal wavenumbers ($m$). The second effect is due to the influence of viscosity, which attenuates perturbations at high wavenumbers. A detailed description of how the correction terms corresponding to these two effects are calculated is given elsewhere (Thompson et al., 2006); the final result for the predicted global viscous growth rate of centrifugal instability is

$$\sigma^* \equiv \sigma U/D = s_o(1 - R_v/mw) - cm^2/(R_v^2\mathrm{Re}). \tag{2}$$

Here, $s_o$ and $w$ are the maximum and halfwidth of the inverse-parabola-like function $s(r)$ in the unstable radial range, rescaled by $U/D$ and $D$, respectively, and $c$ is a dimensionless constant of $\mathcal{O}(1)$. The parameters appearing in this expression can be evaluated from the numerical results and give the following: $s_o = 2.57$, $R_v = 1.25$, $w = 0.1$. The final result of the growth rate curve $\sigma^*(m)$ for the flow considered here is displayed in Fig. 7 for a choice of $c = 2$ (this choice is discussed in more detail in Thompson et al., 2006). The predicted most amplified mode number and maximum growth rate are $m_{\max} = 25$ and $\sigma_{\max} = 0.57$, respectively. Also drawn on this figure, is the growth rate curve obtained from linear stability analysis of the 'frozen' (= forced-to-be-stationary) base flow shown in Fig. 6(a), which gives similar values: $m_{\max} = 19$ and $\sigma_{\max} = 0.53$.

While the results are similar, the analytical prediction based on an idealised axisymmetric flow (in an azimuthal plane) gives a growth curve that is displaced to slightly higher wavenumbers. In reality, the drawn-out secondary vorticity only envelops approximately half of the primary core circumference, and this state is maintained in quasi-equilibrium for some time. In view of this, the stability of the idealised 'frozen' vorticity distribution shown in Fig. 8(a), which captures the main physical characteristics of the real distribution, was investigated. It was obtained by considering an axisymmetric vortex with a vorticity profile given by the azimuthal average of the flow in Fig. 6(a), removing the negative vorticity at the left of the core centre and deriving the associated velocity distribution. The stability was determined numerically using linear stability analysis. The perturbation field distribution is shown in Fig. 8(b), which shows a very similar spatial distribution to that obtained from the direct simulation shown in Fig. 5. In particular, the field has the highest amplitude at the top of the core where the base vorticity changes sign radially. The perturbation field is also strong near the outer edge of the secondary vorticity towards the top of the core, again in agreement with the observed distribution. The corresponding predicted growth rate curve is plotted in Fig. 7. It agrees very well with the actual growth rate curve based on the frozen flow, in terms of shape, the preferred azimuthal mode number and the peak growth rate. Hence, there seems to be strong support for concluding that the three-dimensional instability observed for sphere impact for $\mathrm{Re} \gtrsim 1000$ is due to a centrifugal mechanism.

## 5. Comparison with the impact of an isolated vortex ring

In this section, we investigate in more detail the similarities and differences existing between the sphere impact flow and the collision of an isolated ring vortex with a wall. The experiments by Walker et al. (1987) concerning the latter showed that the vortex ring becomes unstable to a long wavelength instability of azimuthal wavenumber $m \simeq 6$. This instability is clearly seen in their visualizations at $\mathrm{Re}_\Gamma = 2985$ (see the parameter definitions for this flow in Section 2.2). It was associated with the fragmenting secondary vorticity pulled up from the boundary layer as the vortex ring approached the wall and spread out radially. In the direct simulations by Orlandi and Verzicco (1993), forced with an $m = 6$ azimuthal perturbation, again the initial growth of the instability was clearly in the ringlet which fragmented from the secondary vorticity. Swearingen et al. (1995) also performed forced DNS and developed a simplified analytical

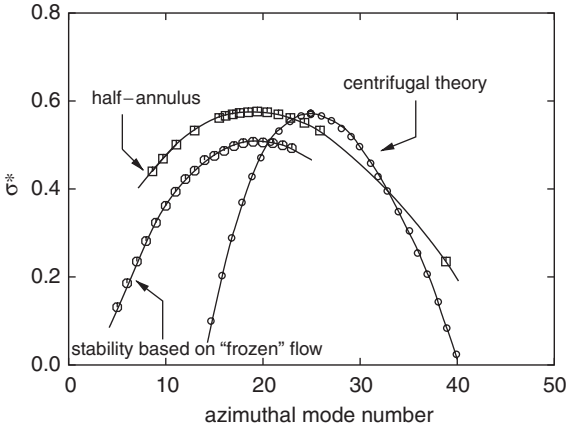


Fig. 7. Global viscous growth rate of centrifugal instability as function of azimuthal wavenumber $m$, for the flow field in Fig. 6(b). Also shown are the growth rate curves obtained from linear stability analysis of the 'frozen' base flow in Fig. 6(a), and the idealized model shown in Fig. 8(a) (labelled half-annulus).

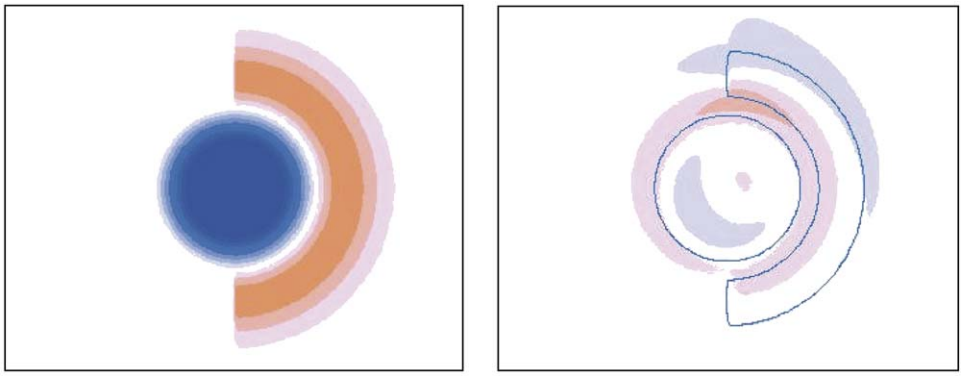


Fig. 8. (a) Idealized vorticity distribution used for the numerical stability analysis. (b) Azimuthal vorticity perturbation field corresponding to the maximally amplified wavelength ($m = 19$).

model, treating the fragmenting secondary vorticity as a set of discrete line vortices. The resulting predictions were consistent with the observed development of the instability in the simulations.

In order to further investigate this point, a series of axisymmetric DNS calculations of an impacting vortex ring were performed, using the same initial configuration as Orlandi and Verzicco (1993), i.e., a vortex ring with a ratio of core to ring radius of $a/A = 0.4131$ at a distance of one ring diameter above the wall. Fig. 9 shows the azimuthal vorticity distributions for a sequence of Reynolds numbers at two nondimensional times. For $\mathrm{Re}_\Gamma = 1500$ (and higher), the development of a discrete secondary ringlet from the enveloping secondary vorticity is clearly apparent. At later times, the ringlet breaks away from the secondary vorticity trail, forming a discrete structure that orbits the primary ring.

Fig. 10 shows visualizations of a vortex ring impact on a wall obtained by three-dimensional DNS for $\mathrm{Re}_\Gamma = 2895$ and the same initial condition as above; it is the case previously investigated numerically by Orlandi and Verzicco (1993), who applied an explicit forcing of an $m = 6$ perturbation to excite the instability. For the current simulation, a low-level white noise perturbation is applied instead at the start of the simulation. The figure shows isosurfaces of both total azimuthal vorticity to highlight the primary vortex structures, and perturbation azimuthal vorticity to reveal the developing perturbation mode. As described above, the primary vortex ring pulls out secondary vorticity from the wall, which fragments into semi-discrete secondary ringlets. This is clearly seen in Fig. 10(a) at $t^* = 30$. At this time, a secondary vortex ringlet of smaller radius exists above the primary ring, and it has developed a clear azimuthal

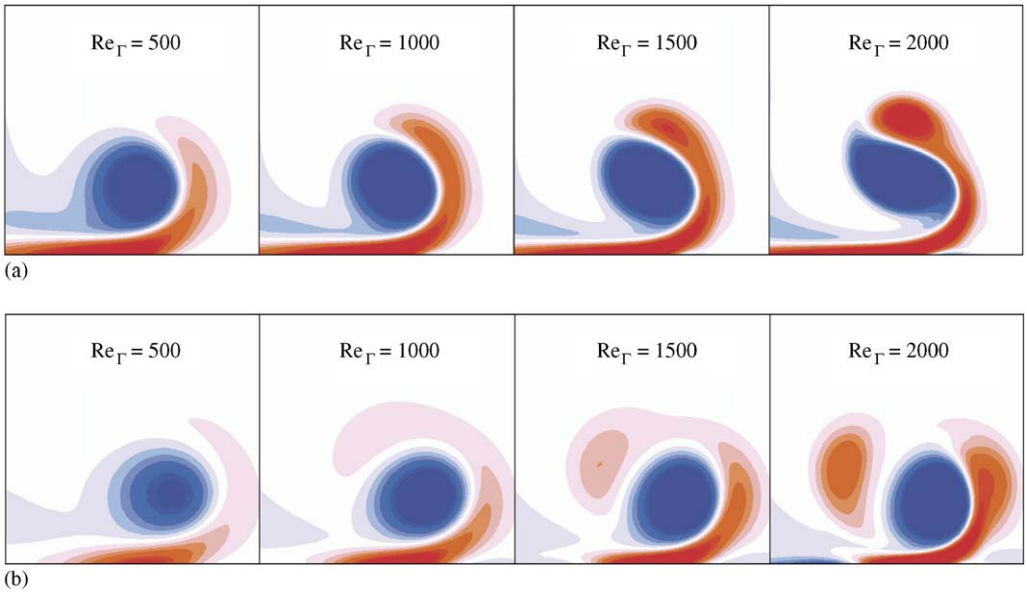


Fig. 9. Azimuthal vorticity for a vortex ring impact at different Reynolds numbers. (a) $t^* = 20$, (b) $t^* = 30$. The field of view has dimensions $2A \times 2A$ and is radially centred at a distance of $2A$ from the symmetry axis of the ring.

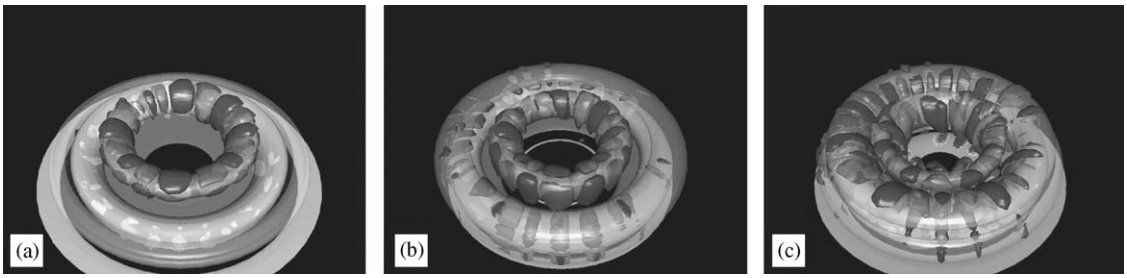


Fig. 10. Development of the azimuthal instability after a vortex ring impact with a wall at $\mathrm{Re}_\Gamma = 2895$. (a) $t^* = 30$, (b) $t^* = 37.5$, (c) $t^* = 45$.

instability mode, with a wavenumber $m \simeq 8$. At a later time, the enveloping secondary azimuthal vorticity surrounding the primary vortex ring also forms a clear azimuthal instability, but with a significantly higher wavenumber $m \simeq 16$. This second instability, which again exhibits the characteristics of a centrifugal mechanism, replaces at later times the initial low-wavenumber mode, which dies out rather rapidly. The existence of this short-wave centrifugal instability in the impacting vortex ring flow is an interesting new observation. It was not detected in previous experimental or numerical studies, possibly due to the characteristics of the initial noise and/or forcing used there. If the initial perturbation is sufficiently large, the breakup of the primary ring will occur through the strong amplification of the low-$m$ mode, and this is often observed in practice, as in the experiments of Walker et al. (1987). One may now conclude that a mechanism analogous to the one leading to three-dimensional instability in the impacting sphere flow is also possible and observable for the impacting vortex ring, and that the two configurations indeed bear a number of similarities.

For a closer comparison, Fig. 11 shows a sequence of azimuthal vorticity fields for a sphere impact. Again, as the Reynolds number is increased, there is a growing tendency of the secondary vorticity to be pulled further around the primary ring. For $\mathrm{Re} = 1500$, there is some indication that the secondary vorticity is beginning to fragment. Interestingly, in the experiments, the ring is observed to develop three-dimensional instabilities for $\mathrm{Re} \gtrsim 1000$, and certainly for $\mathrm{Re} \geqslant 1200$. Thus, for the sphere impact, the three-dimensional centrifugal instability manifests itself at lower Reynolds numbers than those required for significant fragmentation of the enveloping secondary vorticity. This is

not the case for the isolated vortex ring impact, where instability only appears for $\mathrm{Re}_\Gamma \gtrsim 2300$ (Walker et al., 1987), i.e., for values where the secondary vorticity is clearly fragmented (Fig. 9).

At present, the reasons for this somewhat surprising difference in behaviour are not entirely clear. A few hypotheses can be put forward. A first possible explanation involves a difference in the centrifugal instability growth rate between the two cases. Following the analysis in Section 4.2.3, a dimensional analysis of Eq. (1) indicates that the dominant contribution $s_o$ to the inviscid growth rate scales as $\Gamma_p/R^2$, where $\Gamma_p$ is the circulation of the primary vortex and $R$ its radius (i.e., the radius of the quasi-circular line where the vorticity changes sign). Fig. 12 shows $\Gamma_p$ at $\tau = 4$ for the vortex ring produced by the sphere impact, and at $t^* = 20$ for the isolated vortex ring impact. These times both correspond to when the secondary vorticity is lifted from the wall to partially envelop the primary ring, even if they are numerically quite different, due to the different temporal scaling involved. The circulations are obtained by integrating the velocity around a closed contour containing the positive vorticity of the primary ring. It is appropriate to compare the evolution of $\Gamma_p$ with Reynolds number, despite the difference in definition of the latter for the two cases, since the different regimes of secondary vorticity structure and the onset of fragmentation are found in similar ranges of values. Fig. 12 shows that, for $\mathrm{Re} \simeq \mathrm{Re}_\Gamma$, the primary vortex circulations are similar to within about 10%. An estimate of the core radius $R$ can be obtained directly from the vorticity plots in Figs. 9 and 11, taking into account the scalings and the size and position of the field of view. The result is that, for the configurations before the onset of fragmentation ($\mathrm{Re}_{(\Gamma)} = 1000$–$1200$), the primary core (scaled on the ring diameter) of the impacting vortex ring is almost twice as large as the one generated by the sphere impact. With the circulation being almost the same for both cases, this means that the inviscid part of the centrifugal instability growth rate should be roughly 4 times higher for the impacting sphere case. A second difference, potentially relevant for instability growth, is found in the transient evolution of the primary vortex ring. In the sphere case, this vortex ring encounters significant amounts of opposite-signed vorticity when it threads over the sphere, i.e., *before* the actual wall interaction. This means that it is exposed to a centrifugally unstable situation much longer than the isolated impacting vortex ring and that the perturbations have more time to build up.

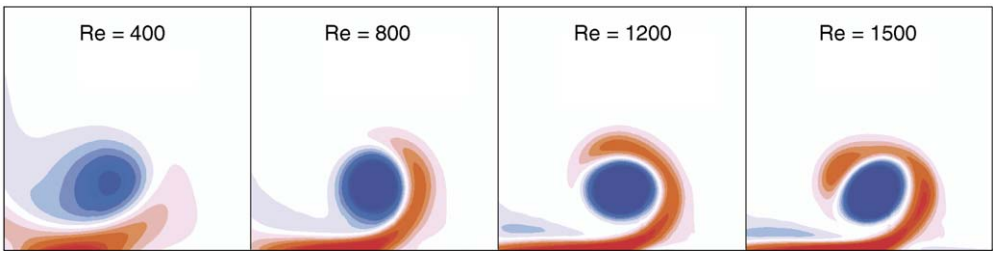


Fig. 11. Azimuthal vorticity for a sphere impact with a wall at different Reynolds numbers. $L/D = 5$ and $\tau = 4$. The field of view has dimensions $1D \times 1D$ and is radially centred at a distance of $1.25D$ from the centre of the sphere.

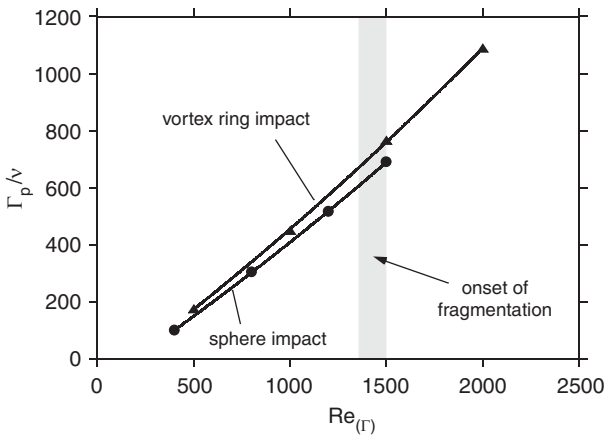


Fig. 12. Comparison of the primary vortex circulation, as function of Re for the sphere impact with $L/D = 5$ at $\tau = 4$, and as function of $\mathrm{Re}_\Gamma$ for the vortex ring impact at $t^* = 20$. Times were chosen so that the secondary vorticity structure is similar in both flows.

Further detailed analysis is needed to understand why exactly the vortex generated by a sphere impact becomes unstable earlier (i.e., *before* fragmentation of the secondary vorticity) than an isolated impacting vortex ring, despite the apparent similarities between the two flows.

## 6. Conclusion

In this paper, physical aspects of the three-dimensional instability of the flow generated by an sphere impacting normally on a solid wall is analysed. Evidence is presented showing that this instability which manifests for Reynolds numbers in excess of about 1000, is consistent with a centrifugal instability associated with the enveloping of the primary vortex ring core with secondary vorticity drawn up from the wall. Both the azimuthal mode numbers and the growth rates, predicted from analytical theory and an idealised physical model, provide a good match to those found in experiments, DNS, and by a linear stability analysis of the frozen flow. Since the primary ring becomes elliptical in cross-section after impact, the flow field was also investigated for an elliptic instability, occurring in strained vortical flows. While the predicted preferred azimuthal mode numbers match well, the predicted growth rate was found to be negative.

Comparisons were made with the flow generated by an isolated vortex ring approaching a wall. In both cases, the vortex ring draws up secondary vorticity, as it moves out radially after impact, and the vorticity patterns are quite similar. Unlike the sphere impact flow, the impacting ring does not become unstable until reaching a Reynolds number high enough for the fragmentation of the secondary vorticity into quasi-discrete secondary vortices. The first fragmented secondary vortex undergoes a deformation at low azimuthal wavenumber ($m \simeq 6$, compared to $m \simeq 20$ for the sphere impact), involving self- and mutual induction from the primary vortex. Interestingly, direct simulations of the vortex ring impact indicate that this growth arrests relatively quickly, and a shorter-wavelength instability takes over, which is observed here for the first time, and which appears to be associated with the centrifugal mechanism. Some arguments why this short-wave instability does not appear for lower Reynolds numbers without fragmentation, as in the impacting sphere case, are presented. These results suggest that, if the initial noise level could be kept sufficiently low in an experiment, the instability responsible for the break-up of the primary ring could change from the longer-wavelength line-vortex instability to the shorter-wavelength instability observed for sphere impacts.

## Acknowledgement

This work was supported by grants from the Australian Research Council (Grant no. LX0242362) and the French CNRS (Grant no. DRI 11721).

## References

Bayly, B.J., 1988. Three-dimensional centrifugal-type instabilities in inviscid two-dimensional flows. Physics of Fluids 31, 56–64.

Eames, I., Dalziel, S.B., 2000. Dust resuspension by the flow around an impacting sphere. Journal of Fluid Mechanics 403, 305–328.

Eloy, C., Le Dizès, S., 1999. Three-dimensional instability of Burgers and Lamb-Oseen vortices in a strain field. Journal of Fluid Mechanics 378, 145–166.

Gondret, P., Lance, M., Petit, L., 2002. Bouncing motion of spherical particles in fluids. Physics of Fluids 14, 643–652.

Joseph, G.G., Zenit, R., Hunt, M.L., Rosenwinkel, A.M., 2001. Particle-wall collisions in a viscous fluid. Journal of Fluid Mechanics 433, 329–346.

Kerswell, R.R., 2002. Elliptical instability. Annual Review of Fluid Mechanics 34, 83–113.

Landman, M.J., Saffman, P.J., 1987. The three-dimensional instability of strained vortices in a viscous fluid. Physics of Fluids 30, 2339–2342.

Leweke, T., Thompson, M.C., Hourigan, K., 2004. Vortex dynamics associated with the collision of a sphere with a wall. Physics of Fluids 16, L74–L77.

Orlandi, P., Verzicco, R., 1993. Vortex rings impinging on walls: axisymmetric and three-dimensional simulations. Journal of Fluid Mechanics 256, 615–646.

Sheard, G.J., Thompson, M.C., Hourigan, K., 2003. From spheres to circular cylinders: classification of transitions and structures of bluff ring wakes. Journal of Fluid Mechanics 492, 147–180.

Swearingen, J.D., Crouch, J.D., Handler, R.A., 1995. Dynamics and stability of a vortex ring impacting a solid boundary. Journal of Fluid Mechanics 297, 1–28.

Thompson, M.C., Leweke, T., Provansal, M., 2001. Kinematics and dynamics of sphere wake transition. Journal of Fluids and Structures 15, 575–585.

Thompson, M.C., Leweke, T., Hourigan, K., 2006. Sphere-wall collision: vortex dynamics and stability. Journal of Fluid Mechanics, submitted for publication.

Walker, J.D., Smith, C.R., Cerra, A.W., Dogilaski, T.L., 1987. The impact of a vortex ring on a wall. Journal of Fluid Mechanics 181, 99–140.

Warburton, T.C., Karniadakis, G.E., 1997. Spectral simulation of flow past a cylinder close to a free surface. ASME Paper FEDSM97-3389.